Chemical Science

ROYAL SOCIETY OF CHEMISTRY

EDGE ARTICLE

View Article Online
View Journal | View Issue

Check for updates

Cite this: *Chem. Sci.*, 2025, **16**, 12332

All publication charges for this article have been paid for by the Royal Society of Chemistry

High-capacity aqueous imidazolium-ion batteries enabled by MMZ-H^+/H^+ co-intercalation in a near neutral electrolyte†

Haiping Yu,[ab] Rui Li,[ab] Zhihui Wang,[c] Bei Wang,[ab] Mengxiao Li,[c] Guoqing Zhao,[c] Xinyu Wang,[ab] Xiaorong Yan,[c] Yuxin Hao,[ab] Huige Ma,[ab] Jingru Liu,[ab] Mingjun Hu *[c] and Jun Yang*[ad]

Received 10th April 2025
Accepted 2nd June 2025

DOI: 10.1039/d5sc02677f

rsc.li/chemical-science

Rechargeable aqueous batteries are regarded as promising candidates for large-scale energy storage with the advantages of cost-effectiveness, environmentally friendliness, and innate safety. However, to date, most of the aqueous ion batteries that have been reported are equipped with metal cation charge carriers and encounter either poor sustainability or low reaction activity. Here, we first reported an aqueous imidazolium-ion battery with MMZ-H^+/H^+ as co-intercalated ions. In detail, we configured an almost neutral electrolyte with a wide electrochemical window of 2.66 V by adding an appropriate amount of alkaline 1-methylimidazole (MMZ) to 0.5 M H_2SO_4, and named it 50M–10S electrolyte. Due to the strong binding energy between MMZ and H^+, MMZ-H^+ as an entire unit can be inserted into or extracted from the HATN-3CN (hexaazatrinaphthalene-2,8,14-tricarbonitrile) electrode. The MMZ-H^+ and H^+ co-insertion increases the capacity by 40% compared to pure H^+ insertion in this proton battery (287.6 mAh g^{-1} in 50M–10S electrolyte *vs.* 206.8 mAh g^{-1} in 0.5 M H_2SO_4 electrolyte, 0.1 A g^{-1}). Theoretical calculations illustrated that the insertion of MMZ-H^+ can further activate the unreacted N active sites due to their enhanced nucleophilicity derived from stronger electron-donating ability of ionized nitrogen sites than the protonated one. Moreover, the assembled full batteries also exhibit ultra-high specific capacity (266.6 mAh g^{-1}, 1 A g^{-1}) and ultra-slow degradation (capacity retention of 97%, 1 A g^{-1}, 1000 cycles). This research further enriches the library of inserted ions and will help to understand and enhance proton storage in near-neutral electrolytes and build new battery models.

Introduction

Rechargeable batteries are attracting widespread attention due to the increasing depletion of fossil fuels.[1,2] Up to now, metal ion batteries, especially Li-ion batteries (LIBs) with non-aqueous electrolytes, have been applied in portable electronics and electric vehicles, for their high energy density and satisfactory cycle life.[3–5] However, lithium as a scarce resource in nature limits the further development of LIBs.[6] Although sodium-ion batteries (SIBs) and potassium-ion batteries (KIBs) with earth-abundant elements as charge carriers are promising candidates,[7,8] the use of flammable electrolytes in these batteries may pose safety risks especially in extreme environments such as crash and needle puncture.[9] Hence, it is necessary to explore aqueous energy storage devices with low cost and high security.

Various aqueous batteries have emerged as a reliable alternative with high-level safety, outstanding rate performance, and low cost.[10–15] Among them, non-metal ions, protons (H^+) and ammonium (NH_4^+) ions, are considered as promising energy storage systems due to their sustainability.[16] However, the electrochemical window of aqueous electrolytes is limited by water decomposition potentials (1.23 V).[17] Although ammonium salt electrolytes are less prone to the hydrogen evolution reaction (HER) compared with strong acid electrolytes,[15] they are commonly afflicted with low electrochemical reaction activity, which gives rise to non-ideal electrode capacity. For protonic electrolytes, other problems that are often mentioned are the dissolution of electrode materials and corrosion of battery packaging materials.[18,19] Recently, water-in-salt (WIS) electrolytes were also developed to widen the electrochemical window by restraining the content of free water, but high viscosity and cost stifled their development potential.[20,21] Similar to the WIS strategy, water-in-acid (WIA) electrolytes with

[a]*Beijing Institute of Nanoenergy & Nanosystems, Chinese Academy of Sciences, Beijing, 101400, China. E-mail: yangjun@binn.cas.cn*

[b]*School of Nanoscience and Engineering, University of Chinese Academy of Sciences, Beijing, 101408, China*

[c]*School of Materials Science and Engineering, Beihang University, Beijing 100191, China. E-mail: mingjunhu@buaa.edu.cn*

[d]*Shenzhen Institute for Advanced Study, University of Electronic Science and Technology of China, Shenzhen, 518000, China*

† Electronic supplementary information (ESI) available. See DOI: https://doi.org/10.1039/d5sc02677f

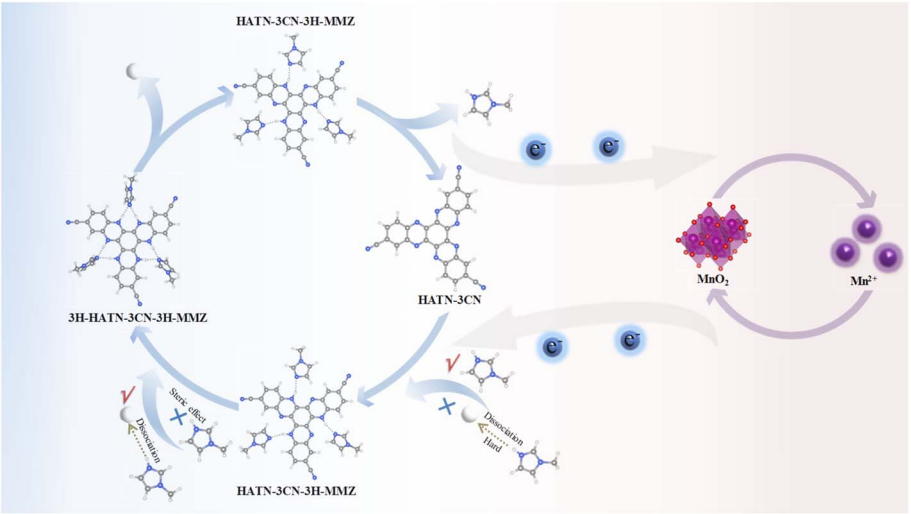

Fig. 1 Scheme of the simplified electrochemical process.

high ionic conductivity have recently been reported. The MoO_3 electrode exhibited a high reversible capacity and excellent cycling stability in a 9.5 M H_3PO_4 electrolyte, fully demonstrating the promising potential of the WIA electrolyte for proton energy storage. However, the corrosiveness of high-concentration H_3PO_4 to metal components and the human body should still not be ignored.[22] Besides, a water-free electrolyte of H_3PO_4/MeCN was proposed to inhibit the hydrogen evolution reaction, but poor compatibility between H_3PO_4 and MeCN results in unstable electrochemical properties of proton batteries.[23] The ionic liquid electrolytes had also been widely researched because of their chemical stability and easy synthesis.[24,25] Nevertheless, the low ion transport rate and high cost limit their popularization.[26] Solid electrolytes have the prospect of commercialization, but the ion transfer efficiency needs to be improved because of the poor interfacial wettability between the electrolyte and the electrode.[27] The addition of organic solvents to aqueous electrolytes is regarded as a useful strategy to broaden the electrochemical stability window while maintaining their non-flammability.[28] However, due to the relatively weak electron-donating ability, most organic solvents showed a very limited influence on proton activity and the hydrogen evolution side reaction of aqueous–organic hybrid electrolyte. Unlike previously reported organic additives, 1-methylimidazole (MMZ) is a potent organic alkali ($pK_a = 6.95$), which can show a strong interaction with protons and thus well regulate proton activity of hybrid electrolytes to inhibit hydrogen evolution and electrode corrosion. However, the intense interaction between MMZ and H^+ ions also suppresses their dissociation and produces a large amount of MMZ-H^+ cations in aqueous electrolytes. Compared to NH_4^+, MMZ-H^+ has a larger size but higher electrode wettability due to the fact that MMZ reduces the interfacial energy between the electrode material and the liquid electrolyte, better increasing the capacity of the electrode.[29] Therefore, it is important to investigate such an aqueous imidazolium-ion battery, not only helping to understand the unique charge storage mechanism in such a proton-pump-like electrolyte, but also promoting the battery performance.

Herein, we configured an electrolyte by an acid-alkali coordinated regulation strategy. The almost neutral electrolyte was prepared by adding a small amount of alkaline MMZ to 0.5 M H_2SO_4, and named it M–S electrolyte. Compared to 0.5 M H_2SO_4, the optimized M–S electrolyte, 50M–10S with a molar ratio of MMZ to H_2SO_4 of 5 : 1, had an 0.71 V wider operating voltage window due to the entrance of MMZ into the solvation sheath of H^+. In addition, this electrolyte with a near-neutral pH value provided the mildest chemical environment, and reduced the chemical dissolution of the electrode materials. More importantly, we found that MMZ could be inserted into the HATN-3CN electrode after protonation (MMZ-H^+), (Fig. 1), which, to the best of our knowledge, is the largest inserted cation reported to date for energy storage (Fig. S1 and Table S1†). A series of characterization studies had verified the co-insertion of MMZ-H^+ and H^+ during electrochemical reactions. The capacity of the HATN-3CN electrode has been increased by 40% compared to pure H^+ insertion (287.6 mAh g^{-1} in 50M–10S electrolyte *vs.* 206.8 mAh g^{-1} in 0.5 M H_2SO_4 electrolyte, 0.1 A g^{-1}), and also far exceeded the capacity in 1 M $(NH_4)_2SO_4$, another near-neutral electrolyte (Fig. S2†). The full batteries were assembled by using MnO_2 as the cathode, HATN-3CN as the anode and 0.5 M $MnSO_4$ + 50M–10S as the electrolyte. High capacity (266.6 mAh g^{-1}, 1 A g^{-1}) and excellent capacity retention (97% capacity retention, 1 A g^{-1}, 1000 cycles) were achieved. This work is expected to provide valuable insights and impetus for the development of mild and effective aqueous battery electrolytes.

Results and discussion

Electrolyte design and discussion

Different ratios of MMZ were added to 0.5 M H_2SO_4 and fully stirred to formulate the stable electrolytes. The detailed molar ratios of each component and pH values of the electrolytes are

displayed in Table S2.† Electrochemical impedance spectroscopy (EIS) was used to investigate the ionic conductivity of the electrolytes (Fig. S3†).[30,31] Observably, the ionic conductivity of the 50M–10S electrolyte (254.4 mS cm^{-1}) was the highest among that of all the electrolytes, even better than that of 0.5 M H_2SO_4 (219.6 mS cm^{-1}), which may be attributed to the increased types and quantities of cations as well as abundant N sites on MMZ for proton hopping.[32] Specifically, the introduction of methylimidazolium, as a weak base, can promote the secondary ionization of HSO_4^- and increase the ion number, further enhancing the ionic conductivity. Meanwhile, the conjugated imidazolium ring structure of methylimidazolium ions enables the delocalization of the positive charge, which effectively reduces the effective charge density of the cations, weakens the electrostatic attraction between cations and anions (*e.g.*, HSO_4^- and SO_4^{2-}), and improves the ionic migration rate. However, excessive additions of MMZ would increase the resistance of ionic transport due to the enlarged solvation structure and the increased solution viscosity, resulting in a decrease in ionic conductivity (Tables S3 and S4†).[33,34] A series of linear sweep voltammetry (LSV) curves of the electrolytes with different MMZ contents were obtained and suggested that the electrochemical window of 0.5 M H_2SO_4 was significantly broadened after adding MMZ (Fig. S4†), but the extension rate gradually slowed down on increasing the MMZ content. Hence, taking both the ionic conductivity and electrochemical stability window into consideration, we selected this electrolyte with a molar ratio of MMZ to H_2SO_4 of 50 : 10 as the research focus in the following studies.

As shown in Fig. 2a, the electrochemical stability window of 50M–10S electrolyte could reach 2.66 V (from −1.07 V to 1.59 V *vs.* Ag/AgCl), with an extension of 0.71 V compared to that of 0.5 M H_2SO_4 (mainly in the anodic regions). To confirm the safety of aqueous–organic hybrid electrolyte, combustion tests were carried out and indicated that the 50M–10S electrolyte was non-inflammable (Fig. S5†). Then the Fourier transform infrared (FTIR) spectra were obtained to investigate the solution structure of the 50M–10S electrolyte (Fig. 2b). Pure H_2O (gray line), H_2O spiked with MMZ (red line), and H_2O spiked with H_2SO_4 (blue line) served as controls for the 50M–10S electrolyte (green line). The peaks at 1522 cm^{-1} and 1108 cm^{-1} were attributed to imidazole ring skeleton vibration and stretching vibration.[35] Peaks at 1050 cm^{-1} and 1205 cm^{-1} correspond to the O=S=O stretching vibration of SO_4.[2–36] The stretching and bending vibration of $-CH_3$ in MMZ could be observed at 2600–3100 cm^{-1} and 1300–1400 cm^{-1}.[35] The presence of these characteristic peaks indicated that each of the raw materials was stabilized in the 50M–10S electrolyte. The Raman spectra similarly confirmed the presence of these characteristic peaks (Fig. S6†). The typical peaks at 3200–3700 cm^{-1} and 1550–1750 cm^{-1} represented the stretching vibration of HO–H and bending vibration of –OH.[36] The peak intensity of H_2O of 50M–10S electrolyte was the weakest, indicating that free water activity was limited by the interaction among the components. The ^1H nuclear magnetic resonance (^1H-NMR) spectra of electrolytes also provided the same result (Fig. 2c and d). The ^1H chemical shifts at 7.52, 7.01 and 6.90 ppm represented the three C–H on the imidazole ring of MMZ. However, their respective movement to 7.94, 7.15 and 7.08 ppm in 50M–10S electrolyte demonstrated that pyridinic N of MMZ captured H^+ from H_2SO_4. The electron-deficient characteristics of protons weakened the original electron cloud density of the imidazole ring in MMZ, which ensured an increase in the ^1H chemical shift of MMZ in 50M–10S electrolyte.

Molecular dynamics (MD) simulations were performed to analyze the solvation structure of the 50M–10S electrolyte. As

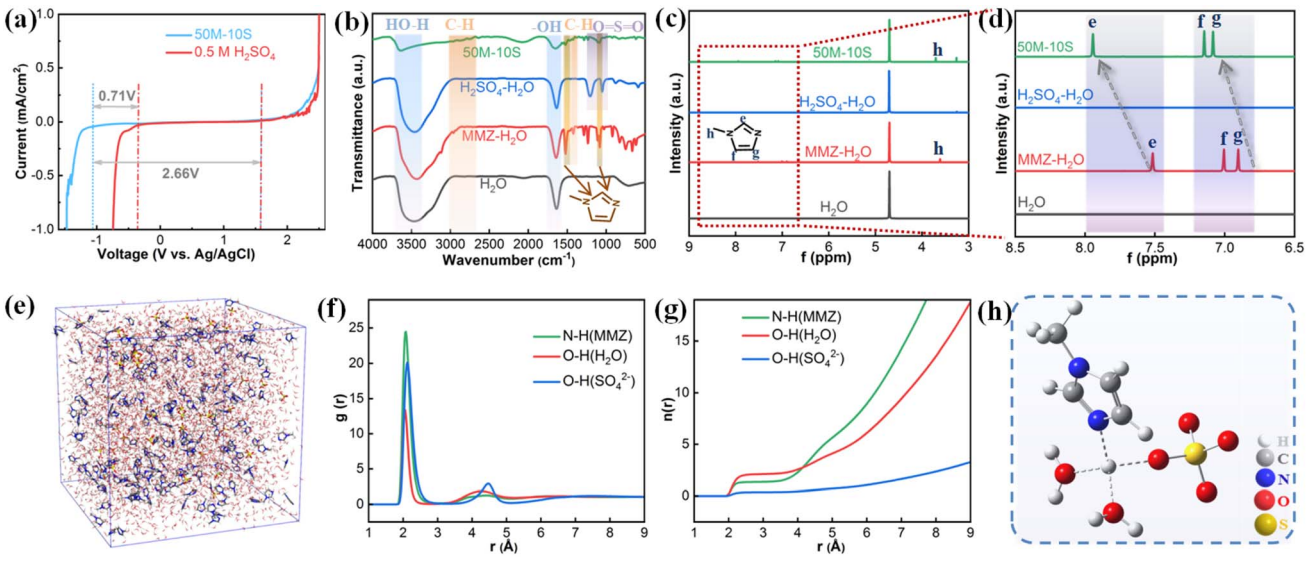

Fig. 2 (a) Electrochemical stability window of 50M–10S electrolyte and 0.5 M H_2SO_4 measured by LSV. The FTIR spectra (b) and ^1H NMR spectra (c and d) of 50M–10S electrolyte and control groups. (e) Snapshot of the MD simulation box of 50M–10S electrolyte. (f) The radial distribution functions (RDFs) of the 50M–10S electrolyte for H–O and H–N. (g) The coordination numbers of H–O and H–N of the 50M–10S electrolyte. (h) Schematic illustration of the H^+ solvation structure in the 50M–10S electrolyte.

shown in Fig. 2e, the snapshot of the 50M–10S electrolyte consisted of 40 H_2SO_4, 200 MMZ and 4320 H_2O molecules. To gain deeper insights into the solvation characteristics, the radial distribution functions (RDFs) were adopted, with the detailed results presented in Fig. 2f. H–N (MMZ), H–O (SO_4^{2-}) and H–O (H_2O) were well identified in the first solvation layer. Significantly, although only a small amount of MMZ was added into the 50M–10S electrolyte, the peak intensity of H–N (MMZ) was the highest, indicating that organic alkali MMZ possessed powerful proton-binding capacity. By integrating the RDFs, the H^+ coordination numbers of the 50M–10S electrolyte were obtained as shown in Fig. 2g. The average coordination number around a single H^+ was about 3.83 in 50M–10S electrolyte, with the contributions being 1.36 from MMZ, 2.11 from H_2O, and 0.36 from SO_4^{2-}, respectively. This indicated that even a modest addition of MMZ was sufficient to change the H^+ solvation sheath, thereby reducing the solvation interaction between water and H^+ (Fig. 2h).[37] Quantum chemistry calculations were performed to obtain the binding energy of several probable solvation structures of 50M–10S electrolyte. Among these configurations, $2H_2O$–1MMZ–$1SO_4^{2-}$–H^+ exhibits an interaction energy of −236.37 kJ mol^{-1}, which corresponds to the highest absolute value. This suggests that its structure is the most stable, which is basically consistent with the solvation structures obtained from MD simulations (Fig. S7a†). Specifically, the high interaction energy of MMZ with H^+ indicated that MMZ-H^+ as a whole was energetically favorable to be inserted into/extracted from the electrodes (Fig. S7b†).

Electrochemical performances

Hexaazatrinaphthalene-2,8,14-tricarbonitrile (HATN-3CN) was used as a model electrode material to prove the charge storage mechanism in such electrolytes. ^{1}H-NMR and High-Resolution Mass Spectrometry (HRMS) of HATN-3CN are displayed in Fig. S8 and S9,† respectively. The powder X-ray diffraction (PXRD) tests indicate that HATN-3CN had good crystalline properties (Fig. S10†). The fiber-rod structure of HATN-3CN could be observed in scanning electron microscope (SEM) and transmission electron microscope (TEM) images (Fig. S11†). The electrochemical performance of HATN-3CN in a Swagelok cell was investigated through taking HATN-3CN, activated carbon (AC), and Ag/AgCl as the working, counter and reference electrodes, respectively. The Nyquist plots of the HATN-3CN electrode showed that the semicircular diameters in these electrolytes were even less than that in pure 0.5 M H_2SO_4 when the molar ratio of MMZ to H_2SO_4 was less than 62.5 : 10 (Fig. 3a and b). It was well illustrated that the addition of a minor amount of MMZ could reduce the charge transfer resistance between electrolyte and the electrode. However, the semicircular diameter increased upon a significant addition of MMZ. This is because the addition of excess MMZ leads to an increased viscosity of the electrolyte, and affects ion transport.[38] Fig. 3c and S12† show the rate performance of the HATN-3CN electrode in the electrolytes with different additions of MMZ at current densities of 0.1–10 A g^{-1}. The electrode in 50M–10S electrolyte exhibited the optimal performance (287.6 mAh g^{-1}, 0.1 A g^{-1}), far better than that in pure 0.5 M H_2SO_4 (206.8 mAh g^{-1}, 0.1 A g^{-1}). According to the principle of solubility similarity, the MMZ ligand of H^+ (MMZ) may show stronger affinity to the HATN-3CN molecules than H_2O and thus better wet the electrode, which will facilitate the (de)insertion dynamics of ions. In contrast, when the H_3O^+ ions approach the surface of the material, due to their poor affinity, some ions may experience ineffective collisions, resulting in a decrease in the overall delivery efficiency.[39] The galvanostatic charge–discharge (GCD) curves of the HATN-3CN electrode in a series of M–S electrolytes are shown in Fig. S13.† The rate specific capacities of the HATN-3CN electrode were found to increase first and then decrease on increasing the MMZ content, with the best result in 50M–10S

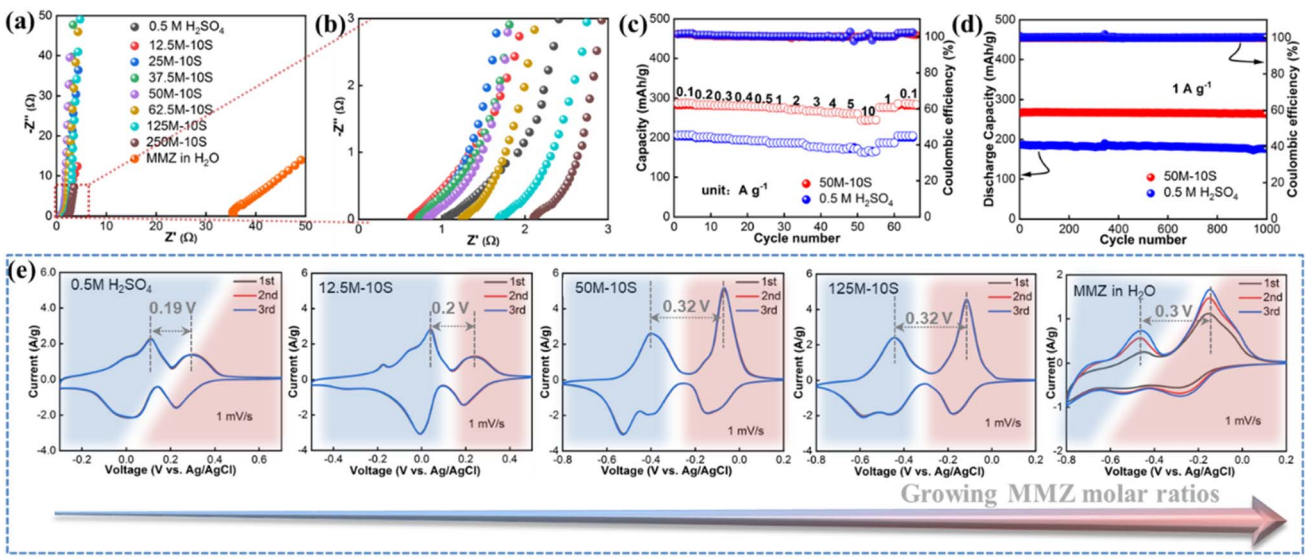

Fig. 3 (a and b) Nyquist plots, (c) rate performance, (d) long-term cycling stability, and (e) CV curves of the HATN-3CN electrode in a series of electrolytes.

electrolyte. The cycling performances of HATN-3CN in 0.5 M H_2SO_4 and 50M–10S electrolyte are shown in Fig. 3d. The capacity slowly decreased to 263.9 mAh g^{-1} with 98.8% capacity retention in 50M–10S electrolyte (1 A g^{-1}, 1000 cycles), which was superior to that in 0.5 M H_2SO_4 electrolyte (94.0% capacity retention, 1 A g^{-1}, 1000 cycles). The GCD curves in the 1st, 10th, 100th, 500th and 1000th cycle are exhibited in Fig. S14a† and the cycle voltammetry (CV) curve after 1000 cycles is shown in Fig. S14b.† Almost constant peak shapes indicated good electrochemical stability of the HATN-3CN electrodes. The obvious fiber-rod structure of HATN-3CN electrodes was clearly visible in the SEM image after 1000 cycles, which also indicated the favorable structural stability of the materials (Fig. S15†). A series of measurements were carried out to probe into the underlying reasons for the enhanced capacity of HATN-3CN in 50M–10S electrolyte. The CV curves of the HATN-3CN electrode are shown in Fig. 3e and S16† in several different M–S electrolytes. With growing MMZ molar ratios, the area of the pair of redox peaks on the right side (corresponding to a higher potential) increased significantly and the potential disparity between the two pairs of redox peaks expanded dramatically. This apparent difference prompted us to hypothesize that a new type of inserted ion (MMZ-H^+) emerges beyond the H^+ due to the addition of MMZ to 0.5 M H_2SO_4. Two sets of experiments were conducted to confirm the availability of MMZ-H^+ insertion. First, we configured the 1 M aqueous solution of 1,3-dimethylimidazolium chloride (1 M DMMZC, pH = 8.23) as the electrolyte. The obvious redox peaks for the HATN-3CN electrode could also be observed and a high specific capacity of 191.1 mAh g^{-1} (0.1 A g^{-1}) was obtained, indicating that large-sized dimethylimidazolium (DMMZ) ions could be inserted into the HATN-3CN electrode but with obvious polarization (Fig. S17a–c†). In addition, a 1-methyl-1,2,4-triazole (MTZ)–H_2SO_4 electrolyte (pH = 6.52) with a similar pH value to the 50M–10S electrolyte was also configured. The MTZ molecule has a similar size to MMZ but exhibited significantly lower basicity. According to previous reports, only hydrogen ions can be inserted into or extracted from electrodes in the MTZ-acid electrolytes.[17,40] Under the same test conditions, the profile of the CV curve for the HATN-3CN electrode in MTZ–H_2SO_4 electrolyte was similar to that in 0.5 M H_2SO_4, indicating that hydrogen ions are the dominant insertion ions in such an electrolyte (Fig. S17d†). The two sets of experiments prove that large-sized DMMZ ions and small-sized hydrogen ions can both be inserted into HATN-3CN electrode but have markedly different reaction dynamics.

Furthermore, a series of characterization methods were performed to verify the assumption that MMZ-H^+ cations might take part in the redox processes. The charge and discharge curves are shown in Fig. 4a and different voltage points were selected for *ex situ* measurements. As shown in Fig. 4b, in the *ex situ* FT-IR spectra, the intensity of the –C=N– peak (1565 cm^{-1}) weakened during the discharge process whereas it was recovered during the charge process.[41] However, no visible change was observed in the peaks of the –C≡N group. This consequence illustrated that –C=N– groups act as the active centers during the redox process rather than –C≡N groups. A similar result was observed in *in situ* Raman spectra (Fig. 4c). The peaks located at 1460 cm^{-1} were attributed to the absorption of the –C–N– group.[42] The change trend of peak intensity of the –C–N– group was the opposite of that of –C=N– during the charging and discharging process, which meant a good reversible conversion between the –C=N– and –C–N– groups.

Subsequently, the *ex situ* X-ray photoelectron spectra (XPS) were used to explore the characteristics of carbon–nitrogen bonding of the HATN-3CN electrode in different voltage states. As shown in Fig. 4d, the –C=N–C– peak was dominant at the pristine state. Upon full discharge, the obvious enhancement of the –C–N– peak (including the –C–N–H peak and –C–N–MMZ-H^+ peak) and the decrease of the –C=N–C– peak indicated that the HATN-3CN electrode was reduced during the discharge process. With the insertion of MMZ-H^+ cations, an emerging –C–N–MMZ-H^+ peak appeared between the –C–N–H peak and –C=N– peak. In addition, due to the electron-withdrawing effect of the proton, a new –C=N–H^+ peak belonging to the protonated MMZ appeared in the position with a higher binding energy than the –C=N–C– peak. After full charging, the –C=N–C– peak became dominant again, the –C–N– peak decreased, and the –C=N–H^+ and –C–N–MMZ-H^+ peaks disappeared, indicating the involvement of MMZ-H^+ as a whole in the charging and discharging process. Besides, the peak of –C≡N was almost constant throughout the charging and discharging process.

To further figure out the charge storage mechanism of the HATN-3CN electrode during charge and discharge, the *ex situ* ^{1}H-NMR spectra were obtained. The H chemical shift values of pure HATN-3CN powder and MMZ were first examined for reference. As shown in Fig. 4e, the ^{1}H chemical shifts of pure HATN-3CN powder at 9.2, 8.7 and 8.4 ppm were labeled as h, i and j, respectively. Similarly, m (9.03 ppm), n (7.69 ppm), o (7.66 ppm) and p (3.88 ppm) were marked in the ^{1}H-NMR spectrum of the 1-methylimidazolium ion (Fig. 4f). Note that to obtain the ^{1}H chemical shifts of the 1-methylimidazolium ion, we tested a series of M–S solutions with different molar ratios of MMZ to H_2SO_4 (Fig. S18†). The ^{1}H resonance signal of the 1-methylimidazolium ion exhibited a progressive downfield shift on increasing the molar ratio of H_2SO_4. Once the molar ratio between MMZ and H_2SO_4 reached 1 : 2, the system attained a state of equilibrium. Subsequent increases in H_2SO_4 content did not significantly change the chemical shift of 1-methylimidazole, confirming full protonation of the imidazole moiety. The invariant δ value was therefore denoted as the ^{1}H chemical shifts of the MMZ-H^+ ions. The evolution of ^{1}H-NMR spectra of HATN-3CN electrodes in 50M–10S electrolyte is shown in Fig. 4g during charging and discharging. In the initial state, three peaks belonging to HATN-3CN are clearly observed in the spectrum. When the electrode was discharged to −0.25 V, the extra peaks of m, n, o, p, and MMZ-H^+ appeared and the intensities increased gradually with the enhanced discharge depth, indicating the insertion of MMZ-H^+. The peaks of MMZ-H^+ and H^+ were both observed in the full discharge state. Moreover, the coordinated H^+ of the inserted MMZ-H^+ ions and the inserted H^+ ions in the HATN-3CN electrode showed the same integrated area. In view of high practical specific capacity of the HATN-3CN electrode (287.6 mAh g^{-1} *vs.* theoretical specific capacity of 350 mAh g^{-1}), 82.2% of the active sites has

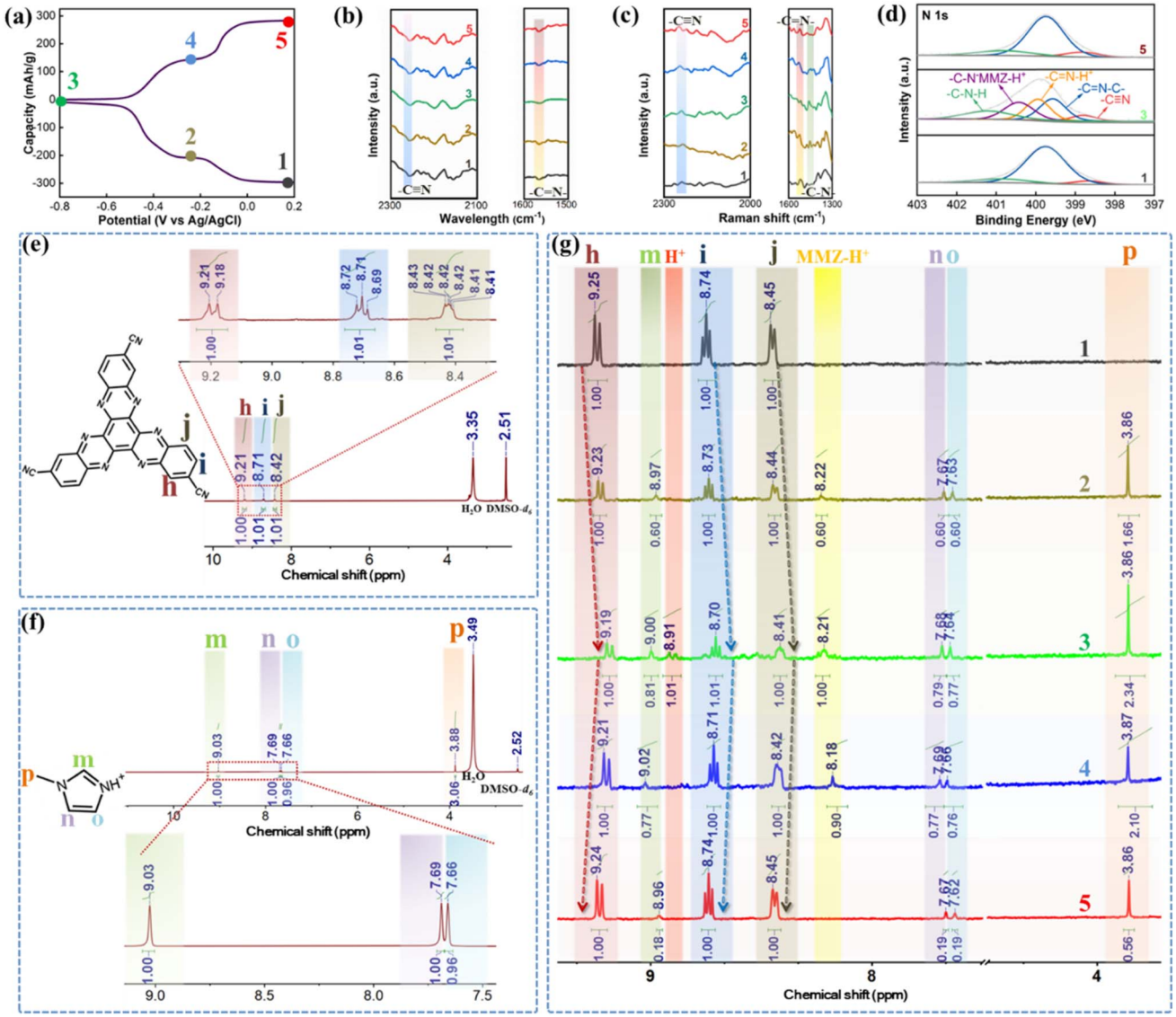

Fig. 4 Energy storage mechanism of HATN-3CN in 50M–10S electrolyte. (a) Indication of different charge and discharge states. (b) *Ex situ* FT-IR spectra. (c) *In situ* Raman spectra. (d) *Ex situ* XPS spectra of N 1s. ^{1}H-NMR spectra of pure HATN-3CN powder (e) and the imidazolium ion (MMZ/H_2SO_4 = 1 : 2) (f). (g) *Ex situ* ^{1}H-NMR spectra. Note: the solvents used for the ^{1}H-NMR spectra were DMSO-d_6 in e–g.

been utilized, and thus it was thought that in 50M–10S electrolyte, three MMZ-H^+ ions and three H^+ ions could be inserted into one HATN-3CN molecule simultaneously. Conversely, in the charge process, along with the increase in the potential, the peak intensities of m, n, o, p, MMZ-H^+ and H^+ decreased gradually. When charged to 0.2 V, the peaks of MMZ-H^+ and H^+ both disappeared and HATN-3CN turned back to its initial state. The increased electromagnetic shielding effect from the electron-rich reduced state intermediate of HATN-3CN was responsible for a decrease in the chemical shift values of h, i, and j.[43] The *ex situ* ^{1}H-NMR spectra of HATN-3CN electrodes in 0.5 M H_2SO_4 are shown in Fig. S19† as the control. In the fully discharged state, only a peak of H^+ was observed and it disappeared with charging, suggesting that the HATN-3CN electrodes underwent mainly reversible insertion and extraction of H^+ in 0.5 M H_2SO_4.

Theoretical calculations based on DFT were used to further comprehend the charge storage process of the HATN-3CN electrode in the 50M–10S and 0.5 M H_2SO_4 electrolytes. Due to cyan group substitution-derived molecular asymmetry, the N active sites of HATN-3CN could be categorized into two groups, named a and b (Fig. S20†). The N active sites belonging to group b had the priority of reaction, based on the adsorption energy calculations. To investigate the type of inserted ions, the energy for the insertion of H^+ derived from the desolvation of MMZ-H^+ and the energy for the insertion of MMZ-H^+ were calculated, respectively (Fig. S21†). The results showed that the insertion of MMZ-H^+ required lower energy, so the HATN-3CN electrode was dominated by the insertion of MMZ-H^+ at the beginning of the discharge. Then, with MMZ-H^+ occupying all b sites, it was no longer possible to insert MMZ-H^+ due to strong steric hindrance (the structure with two MMZ-H^+ inserted in adjacent N

positions cannot be well optimized, Fig. S22†). Therefore, only small-sized H^+ was allowed to be inserted into the HATN-3CN electrode after three b sites were occupied by MMZ-H^+. Since the molar content of MMZ is much higher than H^+ of 0.5 M H_2SO_4 in 50M–10S electrolyte, the vast majority of H^+ is trapped by MMZ. Thus, the direct insertion of free H^+ in the 50M–10S electrolyte is excluded from consideration and H^+ can only be sourced from MMZ-H^+ desolvation. The ion diffusion process in the HATN-3CN electrode during charging and discharging was further explored using the galvanostatic intermittent titration technique (GITT) and EIS. The GITT profiles of the HATN-3CN electrode in 50M–10S electrolyte and 0.5 M H_2SO_4 are shown in Fig. S23a.† The ion diffusion coefficients of the HATN-3CN electrode in 50M–10S electrolyte were high enough (10^{-10}–10^{-9}) compared with that of other reported aqueous electrolytes with various mass transfer ions, although it was an order of magnitude lower than that in 0.5 M H_2SO_4 (10^{-9}–10^{-8}). The faster transport of H^+ than MMZ-H^+ ions may be due to its smaller size and lower hopping energy barrier in the electrode.[44] From the previous characterization studies, it could be seen that both MMZ-H^+ and H^+ were inserted into the HATN-3CN electrode in the 50M–10S electrolyte. If the H^+ is the free H^+ (or hydronium ions) from 50M–10S electrolyte, the ion diffusion coefficients in region 4 corresponding to the (de)insertion of H^+ will be higher than that in region 3 corresponding to extraction of MMZ-H^+, yet the truth was just the opposite (Fig. S23b†). Furthermore, EIS of HATN-3CN at different charge–discharge stages are shown in Fig. S24,† where region 1 and 4 corresponded to the (de)bonding of H^+ and the diffusion of MMZ-H^+ in the HATN-3CN electrode and region 2 and 3 corresponded to insertion/extraction of MMZ-H^+. A similar charge transfer resistance and ion diffusion resistance were observed in different regions, further suggesting that inserted H^+ is derived from the (de)solvation of MMZ-H^+ rather than free H^+ (or hydronium ions) in 50M–10S electrolyte.

DFT calculation was employed to obtain the Gibbs free energy change of ion insertion processes in two paths (Fig. 5a). Path 1 calculated the energy change of free H^+ binding to simulate the electrochemical reduction of the HATN-3CN electrode in 0.5 M H_2SO_4 electrolyte. Similarly, path 2 modeled the energy change of HATN-3CN during the electrochemical reaction in 50M–10S electrolyte. Normally, the more negative the Gibbs free energy, the more probable the reaction is to proceed spontaneously.[45] It was clear that the Gibbs free energies for the last three steps barely changed in path 1, while in path 2 they were significantly reduced, suggesting that a six-electron reaction was more to occur through path 2.[46] The molecular electrostatic potential (MESP) was adopted to identify the electrophilic and nucleophilic reaction-active sites (Fig. S25†).[47] As shown in Fig. 5b, N-atoms of initial HATN-3CN with negative MESP values (the blue region) exhibited higher electronegativity, and were attractive for electrophilic cations (MMZ-H^+ or H^+). However, during the ensuing electrochemical reaction, the MESP results in the two reaction paths are not identical. As shown in Fig. 5c, due to the electron-deficient nature of the H^+, with the insertion of one H^+ into the N sites of HATN-3CN, the

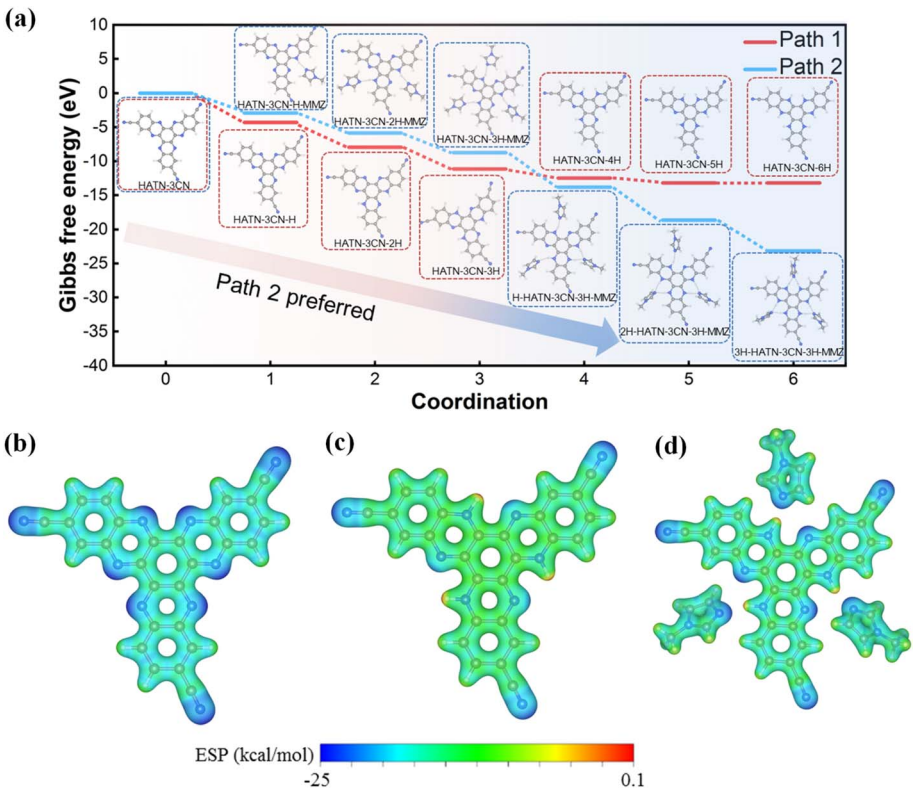

Fig. 5 (a) The Gibbs free energy change at each coordination stage with different ions. Calculation of the MESP distribution of (b) HATN-3CN, (c) HATN-3CN-3H^+ and (d) HATN-3CN-3MMZ-H^+.

nucleophilicity of the neighboring N sites decreased, resulting in a lower reactivity of the unreacted N sites. However, as shown in Fig. 5d, the electron cloud density of the unreacted N active sites of HATN-3CN was significantly higher than that with the insertion of three H^+ because of the stronger electron-donating ability of nitrogen anions combining with MMZ-H^+ cations. This explains the almost unchanged Gibbs free energy in last three steps of path 1, and a significant decrease in Gibbs free energy in path 2 in Fig. 5a. Given the above results, both theory and practice have demonstrated that the involvement of MMZ-H^+ enhances the utilization of the active sites of HATN-3CN electrodes and thus boosts the capacity.

Electrochemical performance of the full cells

Based on the above results, it has been confirmed that the insertion of MMZ-H^+ could enhance the capacity of the HATN-3CN electrode; however, the performance of the full cell remains to be explored. MnO_2, which is cost-effective and easy to synthesize, is selected as the cathode. ε-MnO_2 was synthesized by electrodeposition and evaluated by using the XRD pattern (Fig. S26a†). The SEM images and the energy dispersive spectrometry (EDS) elemental mapping are shown in Fig. S26b.† It can be seen that MnO_2 is uniformly deposited on the surface of the carbon fibers with a homogeneous elemental distribution. The charge–discharge curve of the manganese dioxide electrode revealed a distinct discharge plateau (Fig.-S27a†). This indicates that in our proposed near-neutral electrolyte MnO_2 can show good electrochemical activity. XPS was used to analyze valence characters of the MnO_2 electrode during the charging and discharge process (Fig. S27b†). Mn^{2+} was dominant in Mn 2p spin–orbit peaks after full discharge, which illustrated that a two-electron transfer of manganese was the dominant reaction.[48] The CV curves of the MnO_2 electrode are shown in Fig. S27c.† The redox potential of the MnO_2 electrode in the 0.5 M $MnSO_4$ + 50M–10S electrolyte was lower than that in H_2SO_4 electrolyte, and was similar to that in $Mn(Ac)_2$ electrolyte.[49] Specifically, the reduced electrode potential of MnO_2/Mn^{2+} was related to low H^+ concentration and the reduced Gibbs free energy change. Because of the lower Gibbs free

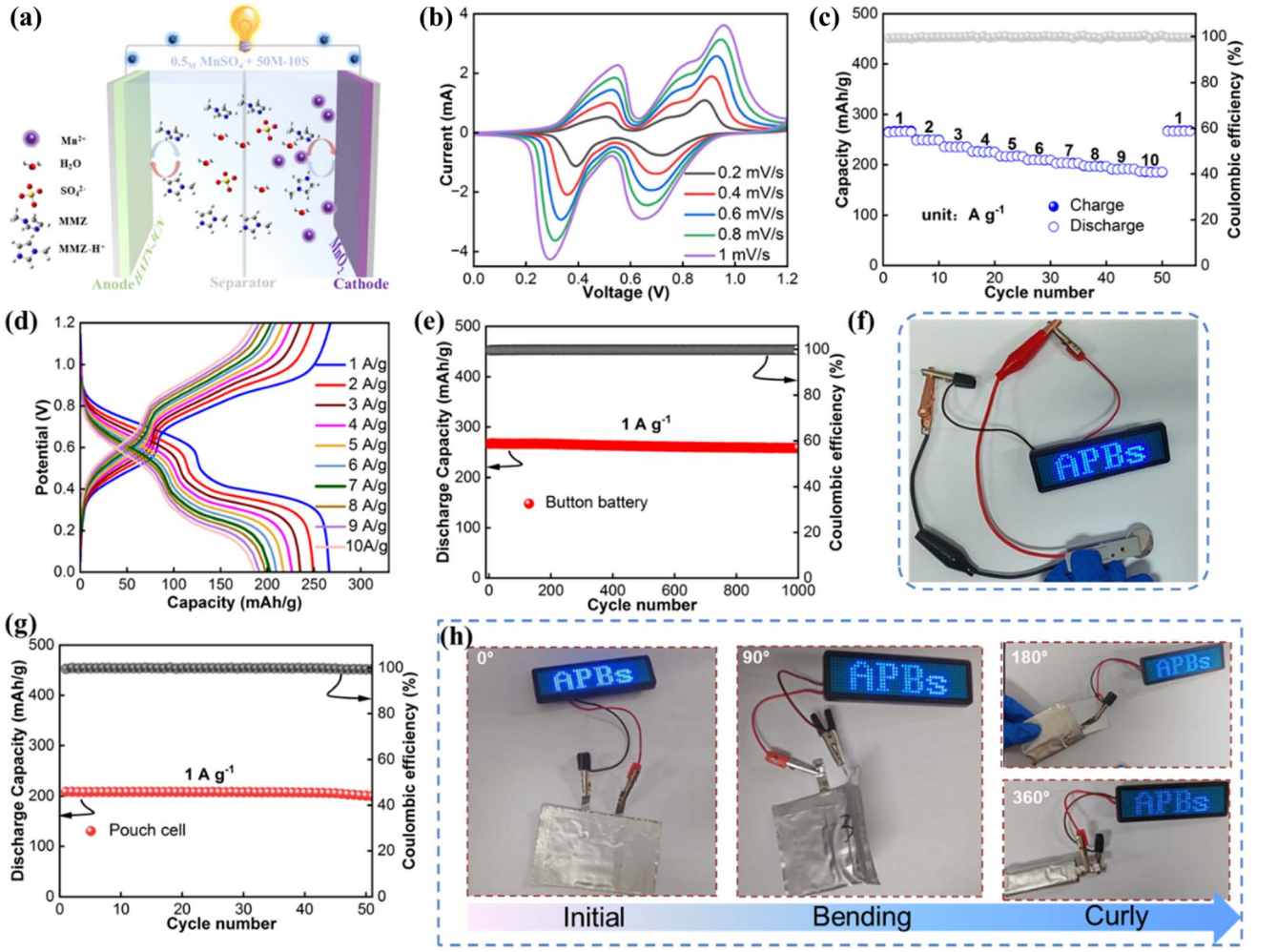

Fig. 6 Electrochemical performance of the HATN-3CN//MnO_2 full battery. (a) Schematic illustration of the full battery. (b) CV curves at different scan rates from 0.2 to 1 mV s^{-1}, (c) rate performance, (d) charge–discharge curves, (e) cycling performance at 1 A g^{-1} and (f) optical image of an LED screen powered by a button-type battery. (g) Cycling performance at 1 A g^{-1} and (h) optical image of an LED screen powered by the pouch cell.

energy of MMZ-H^+ formation compared to the solvated H^+ in H_2SO_4, less energy was required to accomplish the reaction (eqn (1)), and therefore the electrode potential of MnO_2/Mn^{2+} in 50M–10S electrolyte was decreased.

Next, a full cell was assembled by using HATN-3CN as the anode, MnO_2 as the cathode and 0.5 M $MnSO_4$ + 50M–10S as the electrolyte. Considering that 0.5 M $MnSO_4$ + 50M–10S eletrolyte is near-neutral, H^+ and OH^- were avoided to appear in the electrochemical equations. A schematic illustration of a full battery is shown in Fig. 6a, and during charging, Mn^{2+} was oxidized into MnO_2 accompanied by the formation of MMZ-H^+ (eqn (1)). Simultaneously, in the anode, MMZ-H^+ in the electrolyte were inserted into HATN-3CN (eqn (2)). Then H^+ formed by MMZ-H^+ desolvation were inserted into the electrode (eqn (3)). The process was reversed during the discharging process.

$$3Mn^{2+} + 12MMZ + 6H_2O \leftrightarrow 3MnO_2 + 12MMZ\text{-}H^+ + 6e^- \quad (1)$$

$$HATN\text{-}3CN + 3MMZ\text{-}H^+ + 3e^- \leftrightarrow HATN\text{-}3CN\text{-}3H\text{-}MMZ \quad (2)$$

$$HATN\text{-}3CN\text{-}3H\text{-}MMZ + 3MMZ\text{-}H^+ + 3e^- \leftrightarrow 3H\text{-}HATN\text{-}3CN\text{-}3H\text{-}MMZ + 3MMZ \quad (3)$$

The CV curves of the HATN-3CN//MnO_2 full cell were obtained in a potential window of 0–1.2 V, and the obvious reduction and oxidation peaks manifested that the predicted redox reactions have occurred (Fig. 6b). The rate performance of HATN-3CN//MnO_2 was systematically evaluated at various current densities (Fig. 6c). The full battery had a high specific capacity of 266.2 mAh g^{-1} at 1 A g^{-1} (based on the anode mass). Even at a high current density of 10 A g^{-1}, the capacity still remained at 185.8 mAh g^{-1}. When the current density returned to 1 A g^{-1}, the specific capacity recovered to its initial value. These results clearly indicated that the HATN-3CN//MnO_2 battery has fast ion transfer capability and good reversibility. The charge–discharge curves of the HATN-3CN//MnO_2 full cell at various current densities are shown in Fig. 6d, and the results are consistent with those of the CV profiles. Fig. 6e shows the long-term cycle performance of the HATN-3CN//MnO_2 full cell in 0.5 M $MnSO_4$ + 50M–10S electrolyte. The capacity of the full cell decayed very slowly in 0.5 M $MnSO_4$ + 50–10S electrolyte during the cycles, and 97% capacity retention was observed after 1000 cycles at 1 A g^{-1}. In addition, the coulombic efficiency of the full cell remained at around 100% during the 1000 cycles in 0.5 M $MnSO_4$ + 50M–10S electrolyte. This electrochemical performance is excellent compared to that of most reported aqueous ion batteries (Table S5†). The charge–discharge curves during the 1st, 10th, 100th, 500th, and 1000th cycles of the full cell are shown in Fig. S28† in 0.5 M $MnSO_4$ + 50M–10S electrolyte, and the platforms of the curves were distinct and essentially remained unchanged, indicating an excellent cycling stability. The digital image of battery cases after 1000 cycles in 0.5 M $MnSO_4$ + 50M–10S electrolyte is displayed in Fig. S29,† which remained bright and flat after cycling. Fig. S30† presents the digital images of coin cell components after being soaked in the 50M–10S electrolyte for 2 h. Notably, the color of 0.5 M H_2SO_4 solution changed from transparent to shallow green while that of 50M–10S electrolyte remained unchanged. The above results indicate that the addition of a small amount of MMZ to sulfuric acid can reduce the corrosion of the electrolyte on metallic components of button batteries, thus enhancing the compatibility of proton batteries with conventional metal package technology. The HATN-3CN//MnO_2 full cell had a high energy density of 128.0 Wh kg^{-1} at a power density of 480 W kg^{-1} and could light a light-emitting diode (LED) screen at 25 °C (Fig. 6f). The HATN-3CN//MnO_2 pouch cell with high active substance loading still had a high specific capacity of 208.4 mAh g^{-1} at 1 A g^{-1} (based on the anode mass) (Fig. 6g). The CV and GCD curves were similar to those of button cell batteries (Fig. S31†). The pouch cell could light a light-emitting diode (LED) screen after curling and folding (Fig. 6h), indicating the good application potential of 50M–10S electrolyte in aqueous imidazolium-ion batteries. In brief, the cell with the near-neutral pH imidazolyl electrolyte exhibits attractive electrochemical properties and promising applications.

Conclusion

In this work, we first reported an aqueous imidazolium-ion battery with MMZ-H^+/H^+ dual charge carriers. Due to the insertion of MMZ-H^+, the utilization efficiency of the active site of the HATN-3CN electrode was enhanced. The capacity has been increased by 40% compared to pure H^+ transfer (287.6 mAh g^{-1} in 50M–10S electrolyte *vs.* 206.8 mAh g^{-1} in 0.5 M H_2SO_4 electrolyte, 0.1 A g^{-1}), which is comparable or superior to that of classic aqueous metal ion batteries, such as Zn^{2+}, Na^+ and K^+ batteries, not to mention the rate performance.[46,50,51] The assembled MnO_2//HATN-3CN full batteries with MMZ-based neutral electrolyte show superior capacity and stability. These results will shed light on the study of novel electrolyte with low corrosion, a wide voltage window and high ionic conductivity for aqueous batteries as well as open an avenue for the development of sustainable batteries that do not rely on metal ions as charge carriers. More interestingly, the insertion and extraction of such large-size MMZ-H^+ cations in organic electrode materials may provide new opportunities for intercalation chemistry, the preparation of organic 2D materials, and development of new-type ion batteries.

Data availability

The data supporting this article have been included as part of the ESI.†

Author contributions

Conceptualization, M. J. H. and J. Y.; writing – original draft, H. P. Y.; writing – review & editing, M. J. H. and J. Y.; investigation, H. P. Y., R. L., Z. H. W., B. W., M. X. L., G. Q. Z., X. Y. W., X. R. Y., Y. X. H., H. G. M., and J. R. L.; formal analysis, H. P. Y.; funding acquisition, M. J. H. and J. Y.; all authors performed a final check and approved the final version for submission.

Conflicts of interest

The authors declare no conflict of interest.

Acknowledgements

We acknowledge the financial support from the National Natural Science Foundation of China (22371010, 21771017 and 51702009), the "Hundred Talents Program" of the Chinese Academy of Sciences, Fundamental Research Funds for the Central Universities, the Shenzhen Science and Technology Program (JCYJ20210324115412035 JCYJ20210324123202008, JCYJ20210324122803009 and ZDSYS20210813095534001), and the Guangdong Basic and Applied Basic Research Foundation (2021A1515110880).

References

1 Z. Yang, J. Zhang, M. C. W. Kintner-Meyer, X. Lu, D. Choi, J. P. Lemmon and J. Liu, Electrochemical Energy Storage for Green Grid, *Chem. Rev.*, 2011, **111**, 3577–3613.
2 L. E. Blanc, D. Kundu and L. F. Nazar, Scientific Challenges for the Implementation of Zn-Ion Batteries, *Joule*, 2020, **4**, 771–799.
3 M. Li, J. Lu, Z. Chen and K. Amine, 30 Years of Lithium-Ion Batteries, *Adv. Mater.*, 2018, **30**, 1800561.
4 S. Wang, J. Shi, Z. Liu and Y. Xia, Advanced Ether-Based Electrolytes for Lithium-ion Batteries, *Adv. Energy Mater.*, 2024, **14**, 2401526.
5 Z. Wang, R. Li, G. Zhao, X. Yan, X. Wang, H. Yu, Y. Hao, Y. Dai, H. Ma, M. Li, H. Li, M. Yang, B. Wang, J. Liu, M. Hu and Y. Jun, External ligand-free nickel-catalyzed synthesis of polypyrazines towards stable, high-capacity and low-potential sodium ion storage, *Chem. Eng. J.*, 2024, **499**, 155900.
6 Z. Guo, J. Huang, X. Dong, Y. Xia, L. Yan, Z. Wang and Y. Wang, An organic/inorganic electrode-based hydronium-ion battery, *Nat. Commun.*, 2020, **11**, 959.
7 Q. Liu, Z. Hu, W. Li, C. Zou, H. Jin, S. Wang, S. Chou and S.-X. Dou, Sodium transition metal oxides: the preferred cathode choice for future sodium-ion batteries?, *Energy Environ. Sci.*, 2021, **14**, 158–179.
8 W. Zhang, Y. Liu and Z. Guo, Approaching high-performance potassium-ion batteries via advanced design strategies and engineering, *Sci. Adv.*, 2019, **5**, eaav7412.
9 D. Kundu, B. D. Adams, V. Duffort, S. H. Vajargah and L. F. Nazar, A high-capacity and long-life aqueous rechargeable zinc battery using a metal oxide intercalation cathode, *Nat. Energy*, 2016, **1**, 16119.
10 H. Zhang, Y. Tian, W. Wang, Z. Jian and W. Chen, Organic Ammonium Ion Battery: A New Strategy for a Nonmetallic Ion Energy Storage System, *Angew. Chem., Int. Ed.*, 2022, **61**, e202204351.
11 H. Guo, L. Wan, J. Tang, S. Wu, Z. Su, N. Sharma, Y. Fang, Z. Liu and C. Zhao, Stable colloid-in-acid electrolytes for long life proton batteries, *Nano Energy*, 2022, **102**, 107642.
12 R. Li, M. Yang, H. Ma, X. Wang, H. Yu, M. Li, Z. Wang, L. Zheng, H. Li, Y. Hao, M. Hu and J. Yang, A Natural Casein-Based Separator with Brick-and-Mortar Structure for Stable, High-Rate Proton Batteries, *Adv. Mater.*, 2024, **36**, 2403489.
13 M. Yang, Q. Zhao, H. Ma, R. Li, Y. Wang, R. Zhou, J. Liu, X. Wang, Y. Hao, J. Ren, Z. Zheng, N. Zhang, M. Hu, J. Luo and J. Yang, Integrated Uniformly Microporous C4N/Multi-Walled Carbon Nanotubes Composite Toward Ultra-Stable and Ultralow-Temperature Proton Batteries, *Small*, 2023, **19**, 2207487.
14 G. Zhao, X. Yan, Y. Dai, J. Xiong, Q. Zhao, X. Wang, H. Yu, J. Gao, N. Zhang, M. Hu and J. Yang, Searching High-Potential Dihydroxynaphthalene Cathode for Rocking-Chair All-Organic Aqueous Proton Batteries, *Small*, 2024, **20**, 2306071.
15 X. Wu, Y. Qi, J. J. Hong, Z. Li, A. S. Hernandez and X. Ji, Rocking-Chair Ammonium-Ion Battery: A Highly Reversible Aqueous Energy Storage System, *Angew. Chem., Int. Ed.*, 2017, **56**, 13026–13030.
16 A. Kulkarni, C. Padwal, J. MacLeod, P. Sonar, T. Kim and D. Dubal, Toward Safe and Reliable Aqueous Ammonium Ion Energy Storage Systems, *Adv. Energy Mater.*, 2024, **14**, 2400702.
17 H. Ma, M. Yang, R. Li, Y. Wang, L. Zheng, X. Jing, Y. Hao, Y. Dai, J. Gao, M. Hu and J. Yang, An organic acid-alkali coordinately regulated liquid electrolyte enables stable cycling of high-voltage proton battery, *Chem. Eng. J.*, 2024, **486**, 150102.
18 Y. Xu, X. Wu, H. Jiang, L. Tang, K. Y. Koga, C. Fang, J. Lu and X. Ji, A Non-aqueous H3PO4 Electrolyte Enables Stable Cycling of Proton Electrodes, *Angew. Chem., Int. Ed.*, 2020, **59**, 22007–22011.
19 Y. Hao, M. Yang, H. Ma, R. Li, X. Jing, X. Wang, H. Yu, Y. Dai, M. Li, Z. Wang, H. Li, X. Yan, G. Zhao, B. Wang, J. Liu, M. Hu and J. Yang, Natural low corrosive phytic acid electrolytes enable green, ultrafast, stable and high-voltage aqueous proton battery, *Energy Storage Mater.*, 2024, **70**, 103455.
20 M. Liao, X. Ji, Y. Cao, J. Xu, X. Qiu, Y. Xie, F. Wang, C. Wang and Y. Xia, Solvent-free protic liquid enabling batteries operation at an ultra-wide temperature range, *Nat. Commun.*, 2022, **13**, 6064.
21 Y. Wang, T. Wang, S. Bu, J. Zhu, Y. Wang, R. Zhang, H. Hong, W. Zhang, J. Fan and C. Zhi, Sulfolane-containing aqueous electrolyte solutions for producing efficient ampere-hour-level zinc metal battery pouch cells, *Nat. Commun.*, 2023, **14**, 1828.
22 B. Su, J. Deng, Z. Wu, X. Li, J. Li, H. Yu, P. Li, H. Li, L. Yan, L. Zhang, T.-F. Yi, T. Ma and J. Shu, Water-in-Acid Strategy for Corrosion-Free Proton Storage: Phosphoric Acid Electrolyte Engineering Toward Sustainable Aqueous Batteries, *Angew. Chem., Int. Ed.*, 2025, e202505769.
23 M. Liao, Y. Cao, Z. Li, J. Xu, Y. Qi, Y. Xie, Y. Peng, Y. Wang, F. Wang and Y. Xia, VPO4F Fluorophosphates Polyanion Cathodes for High-Voltage Proton Storage, *Angew. Chem., Int. Ed.*, 2022, **61**, e202206635.
24 X. Tang, S. Lv, K. Jiang, G. Zhou and X. Liu, Recent development of ionic liquid-based electrolytes in lithium-ion batteries, *J. Power Sources*, 2022, **542**, 231792.
25 C. Karlsson, C. Strietzel, H. Huang, M. Sjödin and P. Jannasch, Nonstoichiometric Triazolium Protic Ionic

Liquids for All-Organic Batteries, *ACS Appl. Energy Mater.*, 2018, **1**, 6451–6462.

26 M. Armand, F. Endres, D. R. MacFarlane, H. Ohno and B. Scrosati, Ionic-liquid materials for the electrochemical challenges of the future, *Nat. Mater.*, 2009, **8**, 621–629.

27 Q. Zhao, S. Stalin and L. A. Archer, Stabilizing metal battery anodes through the design of solid electrolyte interphases, *Joule*, 2021, **5**, 1119–1142.

28 P. Liang, S. Di, Y. Zhu, Z. Li, S. Wang and L. Li, Realization of Long-Life Proton Battery by Layer Intercalatable Electrolyte, *Angew. Chem., Int. Ed.*, 2024, **63**, e202409871.

29 L. Zhao, Y. Li, M. Yu, Y. Peng and F. Ran, Electrolyte-Wettability Issues and Challenges of Electrode Materials in Electrochemical Energy Storage, Energy Conversion, and Beyond, *Adv. Sci.*, 2023, **10**, 2300283.

30 C. Karlsson and P. Jannasch, Highly Conductive Nonstoichiometric Protic Poly(ionic liquid) Electrolytes, *ACS Appl. Energy Mater.*, 2019, **2**, 6841–6850.

31 S. Wu, J. Chen, Z. Su, H. Guo, T. Zhao, C. Jia, J. Stansby, J. Tang, A. Rawal, Y. Fang, J. Ho and C. Zhao, Molecular Crowding Electrolytes for Stable Proton Batteries, *Small*, 2022, **18**, 2202992.

32 M. Zhang, H. Hua, P. Dai, Z. He, L. Han, P. Tang, J. Yang, P. Lin, Y. Zhang, D. Zhan, J. Chen, Y. Qiao, C. C. Li, J. Zhao and Y. Yang, Dynamically Interfacial pH-Buffering Effect Enabled by N-Methylimidazole Molecules as Spontaneous Proton Pumps toward Highly Reversible Zinc-Metal Anodes, *Adv. Mater.*, 2023, **35**, 2208630.

33 H. Wang, R. Emanuelsson, C. Karlsson, P. Jannasch, M. Strømme and M. Sjödin, Rocking-Chair Proton Batteries with Conducting Redox Polymer Active Materials and Protic Ionic Liquid Electrolytes, *ACS Appl. Mater. Interfaces*, 2021, **13**, 19099–19108.

34 R. Wang, Q. Ma, L. Zhang, Z. Liu, J. Wan, J. Mao, H. Li, S. Zhang, J. Hao, L. Zhang and C. Zhang, An Aqueous Electrolyte Regulator for Highly Stable Zinc Anode Under −35 to 65 °C, *Adv. Energy Mater.*, 2023, **13**, 2302543.

35 T. Yamada and M. Mizuno, Infrared Spectroscopy in the Middle Frequency Range for Various Imidazolium Ionic Liquids—Common Spectroscopic Characteristics of Vibrational Modes with In-Plane +C(2)–H and +C(4,5)–H Bending Motions and Peak Splitting Behavior Due to Local Symmetry Breaking of Vibrational Modes of the Tetrafluoroborate Anion, *ACS Omega*, 2021, **6**, 1709–1717.

36 Y. Shang, S. Chen, N. Chen, Y. Li, J. Lai, Y. Ma, J. Chen, F. Wu and R. Chen, A universal strategy for high-voltage aqueous batteries via lone pair electrons as the hydrogen bond-breaker, *Energy Environ. Sci.*, 2022, **15**, 2653–2663.

37 J. Hao, L. Yuan, C. Ye, D. Chao, K. Davey, Z. Guo and S.-Z. Qiao, Boosting Zinc Electrode Reversibility in Aqueous Electrolytes by Using Low-Cost Antisolvents, *Angew. Chem., Int. Ed.*, 2021, **60**, 7366–7375.

38 H. Tu, Z. Wang, J. Xue, Z. Tang, Y. Liu, X. Liu, L. Liu, S. Lu, S. Weng, Y. Gao, G. Sun, Z. Liu, K. Peng, X. Zhang, D. Li, G. Wu, M. Liu, J. Hu, H. Li, J. Xu and X. Wu, Regulating Non-Equilibrium Solvation Structure in Locally Concentrated Ionic Liquid Electrolytes for Wide-Temperature and High-Voltage Lithium Metal Batteries, *Angew. Chem., Int. Ed.*, 2024, e202412896.

39 Z. Song, L. Wang, W. Jiang, M. Pei, B. Li, R. Mao, S. Liu, T. Zhang, X. Jian and F. Hu, "Like Compatible Like" Strategy Designing Strong Cathode-Electrolyte Interface Quasi-Solid-State Lithium–Sulfur Batteries, *Adv. Energy Mater.*, 2024, **14**, 2302688.

40 H. Ma, M. Yang, R. Li, L. Zheng, Y. Hao, H. Li, M. Li, G. Zhao, Z. Wang, B. Wang, M. Hu and J. Yang, An Organic Acid-Alkali Coregulated Ionic Liquid Electrolyte Enabling Wide-Temperature-Range Proton Battery, *Small*, 2024, 2405004.

41 Z. Ye, S. Xie, Z. Cao, L. Wang, D. Xu, H. Zhang, J. Matz, P. Dong, H. Fang, J. Shen and M. Ye, High-rate aqueous zinc-organic battery achieved by lowering HOMO/LUMO of organic cathode, *Energy Storage Mater.*, 2021, **37**, 378–386.

42 M. Shi, J. He, Y. Zhao, L. Zhao, K. Dai and C. Yan, *In-situ* Raman investigation and application of phenazine-based organic electrode in aqueous proton batteries, *Mater. Des.*, 2022, **222**, 111043.

43 X. Song, Y. Ge, H. Xu, S. Bao, L. Wang, X. Xue, Q. Yu, Y. Xing, Z. Wu, K. Xie, T. Zhu, P. Zhang, Y. Liu, Z. Wang, Z. Tie, J. Ma and Z. Jin, Ternary Eutectic Electrolyte-Assisted Formation and Dynamic Breathing Effect of the Solid-Electrolyte Interphase for High-Stability Aqueous Magnesium-Ion Full Batteries, *J. Am. Chem. Soc.*, 2024, **146**, 7018–7028.

44 W. Sun, F. Wang, S. Hou, C. Yang, X. Fan, Z. Ma, T. Gao, F. Han, R. Hu, M. Zhu and C. Wang, Zn/MnO2 Battery Chemistry With H+ and Zn2+ Coinsertion, *J. Am. Chem. Soc.*, 2017, **139**, 9775–9778.

45 C. Wu, X. Yan, H. Yu, T. Li, J. Xiong, Y. Dai, Q. Guo, J. Liu, G. Shan, M. Hu and J. Yang, Engineering strong electronegative nitrogen-rich porous organic polymer for practical durable lithium-sulfur battery, *J. Power Sources*, 2022, **551**, 232212.

46 Y. Lin, H. Cui, C. Liu, R. Li, S. Wang, G. Qu, Z. Wei, Y. Yang, Y. Wang, Z. Tang, H. Li, H. Zhang, C. Zhi and H. Lv, Inside Back Cover: A Covalent Organic Framework as a Long-life and High-Rate Anode Suitable for Both Aqueous Acidic and Alkaline Batteries, *Angew. Chem., Int. Ed.*, 2023, **62**, e202302702.

47 Q. Zhao, W. Huang, Z. Luo, L. Liu, Y. Lu, Y. Li, L. Li, J. Hu, H. Ma and J. Chen, High-capacity aqueous zinc batteries using sustainable quinone electrodes, *Sci. Adv.*, 2018, **4**, eaao1761.

48 Z.-H. Huang, Y. Song, D.-Y. Feng, Z. Sun, X. Sun and X.-X. Liu, High Mass Loading MnO2 with Hierarchical Nanostructures for Supercapacitors, *ACS Nano*, 2018, **12**, 3557–3567.

49 C. Xie, T. Li, C. Deng, Y. Song, H. Zhang and X. Li, A highly reversible neutral zinc/manganese battery for stationary energy storage, *Energy Environ. Sci.*, 2020, **13**, 135–143.

50 S. Wu, H. Guo, Z. Su, C. Jia, X. Zhang, S. Wang, T. Zhao, Q. Meyer and C. Zhao, Suppressed Manganese Oxides Shuttling in Acidic Electrolytes Extends Shelf-Life of Electrolytic Proton Batteries, *Adv. Funct. Mater.*, 2024, **34**, 2315706.

51 Y. Liang, Y. Jing, S. Gheytani, K.-Y. Lee, P. Liu, A. Facchetti and Y. Yao, Universal quinone electrodes for long cycle life aqueous rechargeable batteries, *Nat. Mater.*, 2017, **16**, 841–848.